

Full length article

# Spatiotemporal control of myofibroblast activation in acoustically-responsive scaffolds via ultrasound-induced matrix stiffening



Easton Farrell<sup>a,b</sup>, Mitra Aliabouzar<sup>a</sup>, Carole Quesada<sup>a</sup>, Brendon M. Baker<sup>b</sup>, Renny T. Franceschi<sup>b,c</sup>, Andrew J. Putnam<sup>b</sup>, Mario L. Fabiilli<sup>a,c,d,\*</sup>

<sup>a</sup> Department of Radiology, University of Michigan, Ann Arbor, MI, USA

<sup>b</sup> Department of Biomedical Engineering, University of Michigan, Ann Arbor, MI, USA

<sup>c</sup> Dental School, University of Michigan, Ann Arbor, MI, USA

<sup>d</sup> Applied Physics Program, University of Michigan, Ann Arbor, MI, USA

## ARTICLE INFO

### Article history:

Received 11 August 2021

Revised 2 November 2021

Accepted 15 November 2021

Available online 20 November 2021

### Keywords:

Acoustic droplet vaporization

Ultrasound

Phase-shift emulsion

Fibrin

Strain stiffening

Fibroblast

Myofibroblast

Differentiation

## ABSTRACT

Hydrogels are often used to study the impact of biomechanical and topographical cues on cell behavior. Conventional hydrogels are designed *a priori*, with characteristics that cannot be dynamically changed in an externally controlled, user-defined manner. We developed a composite hydrogel, termed an acoustically-responsive scaffold (ARS), that enables non-invasive, spatiotemporally controlled modulation of mechanical and morphological properties using focused ultrasound. An ARS consists of a phase-shift emulsion distributed in a fibrin matrix. Ultrasound non-thermally vaporizes the emulsion into bubbles, which induces localized, radial compaction and stiffening of the fibrin matrix. In this *in vitro* study, we investigate how this mechanism can control the differentiation of fibroblasts into myofibroblasts, a transition correlated with substrate stiffness on 2D substrates. Matrix compaction and stiffening was shown to be highly localized using confocal and atomic force microscopies, respectively. Myofibroblast phenotype, evaluated by  $\alpha$ -smooth muscle actin ( $\alpha$ -SMA) immunocytochemistry, significantly increased in matrix regions proximal to bubbles compared to distal regions, irrespective of the addition of exogenous transforming growth factor- $\beta$ 1 (TGF- $\beta$ 1). Introduction of the TGF- $\beta$ 1 receptor inhibitor SB431542 abrogated the proximal enhancement. This approach providing spatiotemporal control over biophysical signals and resulting cell behavior could aid in better understanding fibrotic disease progression and the development of therapeutic interventions for chronic wounds.

## Statement of Significance

Hydrogels are used in cell culture to recapitulate both biochemical and biophysical aspects of the native extracellular matrix. Biophysical cues like stiffness can impact cell behavior. However, with conventional hydrogels, there is a limited ability to actively modulate stiffness after polymerization. We have developed an ultrasound-based method of spatiotemporally-controlling mechanical and morphological properties within a composite hydrogel, termed an acoustically-responsive scaffold (ARS). Upon exposure to ultrasound, bubbles are non-thermally generated within the fibrin matrix of an ARS, thereby locally compacting and stiffening the matrix. We demonstrate how ARSs control the differentiation of fibroblasts into myofibroblasts in 2D. This approach could assist with the study of fibrosis and the development of therapies for chronic wounds.

© 2021 Acta Materialia Inc. Published by Elsevier Ltd. All rights reserved.

\* Corresponding author at: University of Michigan, 1301 Catherine Street, 3226A Medical Sciences Building I, Ann Arbor, MI 48109-5667, USA.

E-mail address: [mfabiilli@umich.edu](mailto:mfabiilli@umich.edu) (M.L. Fabiilli).

## 1. Introduction

Cells respond to biophysical cues from their surrounding extracellular matrix. For example, lineage specification of mesenchymal stem cells is dependent on matrix stiffness [1–3]. Cancer cells display stiffness-dependent gene regulation that impacts response to

chemotherapeutics [4] and potential for metastasis [5]. The extracellular matrix has a critical role in mechanotransduction, varying spatiotemporally based on homeostatic and pathological events [6]. Hydrogels are used in 2D/3D cell culture to recapitulate both biochemical and biophysical aspects of the native extracellular matrix [7]. Additionally, hydrogels are often utilized for the delivery and implantation of cells for tissue regeneration [8] as well as in the development of tumor models [9]. The stiffness of a hydrogel can be altered by changing the crosslinking density of the polymer network. However, with a conventional hydrogel, there is a limited ability to actively modulate the stiffness after polymerization.

Hydrogels whose biophysical properties can be spatiotemporally modulated can facilitate the study of dynamic biophysical cues on cell behavior [10]. One commonly-used approach is the incorporation of photosensitive molecules within a hydrogel, enabling control of crosslinking using ultraviolet light [11]. A previous study used a dual crosslinking method and a photomask to spatially pattern methacrylated hyaluronic acid hydrogels with elastic moduli from 3 kPa to 100 kPa, which impacted the morphology and proliferation of mesenchymal stem cells [12]. Conversely, ultraviolet light was also used to spatially pattern soft regions within poly(ethylene glycol)-based hydrogels, which impacted activation of YAP in mesenchymal stem cells [13].

Despite its high spatiotemporal resolution, light has a limited ability to penetrate into tissues. This could hinder the on-demand modulation of photocrosslinkable or photodegradable hydrogels after *in vivo* implantation. As an alternative, we have developed composite hydrogels, termed acoustically-responsive scaffolds (ARSs), that can be controlled using focused ultrasound in the megahertz range [14]. An ARS consists of phase-shift emulsion embedded within a hydrogel matrix. The phase-shift emulsion contains a perfluorocarbon (PFC) liquid that vaporizes into a gas bubble when exposed to ultrasound in a mechanism known as acoustic droplet vaporization (ADV) [15,16]. Gas bubbles are formed non-thermally within the PFC phase due to the rarefactional phase of the acoustic wave in combination with the use of an extremely low duty cycle [17,18].

We previously demonstrated in fibrin-based ARSs that the fibrin surrounding each ADV-generated bubble becomes radially compacted [19], which decreased the local matrix porosity [20]. Based on atomic force microscopy, these consolidated regions of fibrin surrounding the bubble possessed significantly greater Young's moduli compared to regions far from bubbles. For example, within one hour of ADV, there was a 70% increase in stiffness adjacent to a bubble compared to distal regions. Based on the subsequent growth of a bubble due to in-gassing, matrix regions proximal to the bubble exhibited a 20-fold increase in elastic modulus compared to distal regions four days after ADV. These results are consistent with the strain stiffening behavior of fibrin [21].

ARSs have been used for the delivery of bioactive molecules whereby ADV released a payload encapsulated within the phase-shift emulsion [22–24]. However, the ability of ADV to modulate cell behavior within an ARS based on ADV-induced changes to the hydrogel matrix has not been explored. In this study, we investigate how ADV-induced matrix stiffening can spatiotemporally modulate differentiation of fibroblasts into myofibroblasts (Fig. 1), a transition that has been shown to be stiffness dependent in 2D culture [25]. Myofibroblasts are a fibroblast sub-type critical to the wound healing process, orchestrating wound closure through contractile behavior and deposition of collagenous matrix [26–28]. However, the sustained presence of myofibroblasts and excess production of matrix is known to contribute to fibrotic scarring, tissue contractures, and organ dysfunction in myocardium, lungs, and intestines, amongst many others [29–31]. Additionally, certain pathologies (e.g., idiopathic pulmonary fibrosis [32]) are characterized by spatial heterogeneity of scar tissue and normal

parenchyma. Conversely, insufficient levels of myofibroblasts have been implicated in the persistence of chronic wounds such as ulcers [33]. Chemical agonists of myofibroblast fate have also been previously established. For instance, cytokines such as transforming growth factor- $\beta$ 1 (TGF- $\beta$ 1) and tumor necrosis factor- $\alpha$  (TNF- $\alpha$ ) induce a myofibroblast phenotype in resident tissue fibroblasts [34–39]. However, the interplay of mechanical and chemical stimuli on fibroblast phenotype is not fully understood.

Here, we used confocal microscopy to characterize the impact of ADV on the microstructure of fibrin in an ARS and atomic force microscopy to map the ADV-induced mechanical changes. Next, fibroblasts were seeded on substrates with defined stiffnesses to assess baseline cell proliferation and  $\alpha$ -smooth muscle actin ( $\alpha$ -SMA) expression, a marker of myofibroblast phenotype. We then seeded fibroblasts on fibrin-based ARSs and evaluated the impact of ADV-generated bubbles, which were produced using different ultrasound exposure conditions, as well as the effect of exogenous TGF- $\beta$ 1 and TGF- $\beta$ 1 receptor inhibitor on  $\alpha$ -SMA expression.

## 2. Materials and methods

### 2.1. Preparation of phase-shift emulsions

Micron-sized, monodispersed phase-shift emulsions ( $W_1$ /PFC/ $W_2$ ) were prepared using a microfluidic-based technique as described previously [23]. Briefly, the  $W_1$  phase consisted of phosphate buffered saline (PBS, Life Technologies, Grand Island, NY, USA) and the PFC phase was perfluoroheptane ( $C_7F_{16}$ , CAS# 335-57-9, Sigma-Aldrich, St. Louis, MO, USA). The primary emulsion (i.e.,  $W_1$ /PFC) was stabilized by 2% (w/w) triblock fluorosurfactant consisting of Krytox 157FSH (CAS# 51798-33-5, DuPont, Wilmington, DE, USA) and polyethylene glycol (1000 g/mol, CAS#: 24991-53-5, Alfa Aesar, Ward Hill, MA, USA). The  $W_2$  phase was 50 mg/mL Pluronic F68 (CAS# 9003-11-6, Sigma-Aldrich) in PBS. The emulsion was characterized using a Coulter Counter (Multisizer 4, Beckman Coulter, Brea, CA, USA) with a 50  $\mu$ m aperture tube. The average diameter, coefficient of variation, and number concentration of the emulsion were  $12.98 \pm 0.8 \mu$ m,  $3.3 \pm 0.9\%$ , and  $(3.5 \pm 0.3) \times 10^8$  particles /mL, respectively.

### 2.2. Formation of ARSs

ARSs were prepared by modifying a previously described method [40]. Bovine fibrinogen (Sigma-Aldrich) was dissolved at 5 mg/mL clottable protein in Dulbecco's modified Eagle's medium (DMEM, Life Technologies). The fibrinogen solution was degassed under vacuum to facilitate solubilization of the fibrinogen and to minimize dissolved gas. ARSs (total volume: 0.5 mL, diameter: 15 mm, height:  $\sim$ 3 mm) were polymerized in 24-well BioFlex plates (Flexcell International Co., Hillsborough, NC, USA) such that the final concentrations of fibrin, bovine lung aprotinin (Sigma-Aldrich), emulsion, and recombinant human thrombin (Recothrom, Baxter, Deerfield, IL, USA) were 4.5 mg/mL, 0.05 U/mL, 0.01% (v/v) (i.e.,  $\sim 3.5 \times 10^4$  droplets/mL), and 2 U/mL, respectively. Fibrin-only gels (i.e., without emulsion) were prepared similarly. Acellular ARS prepared for confocal microscopy analysis also contained 39  $\mu$ g/mL Alexa Fluor 647-labeled fibrinogen (fibrinogen<sub>647</sub>, F35200, Molecular Probes, Eugene, OR, USA). ARSs were then covered with 0.5 mL overlying media consisting of DMEM supplemented with 100 U/mL penicillin, 100  $\mu$ g/mL streptomycin, and 2.5  $\mu$ g/mL amphotericin B (Life Technologies). For optical and mechanical characterization of acellular ARS, each well in the BioFlex plate was coated with 1% (w/v) solution of bovine serum albumin (CAS# 9048-46-8, Sigma-Aldrich) in PBS (for  $\sim$ 30 minutes) prior to polymerization of the ARS to facilitate removal of the scaffolds.

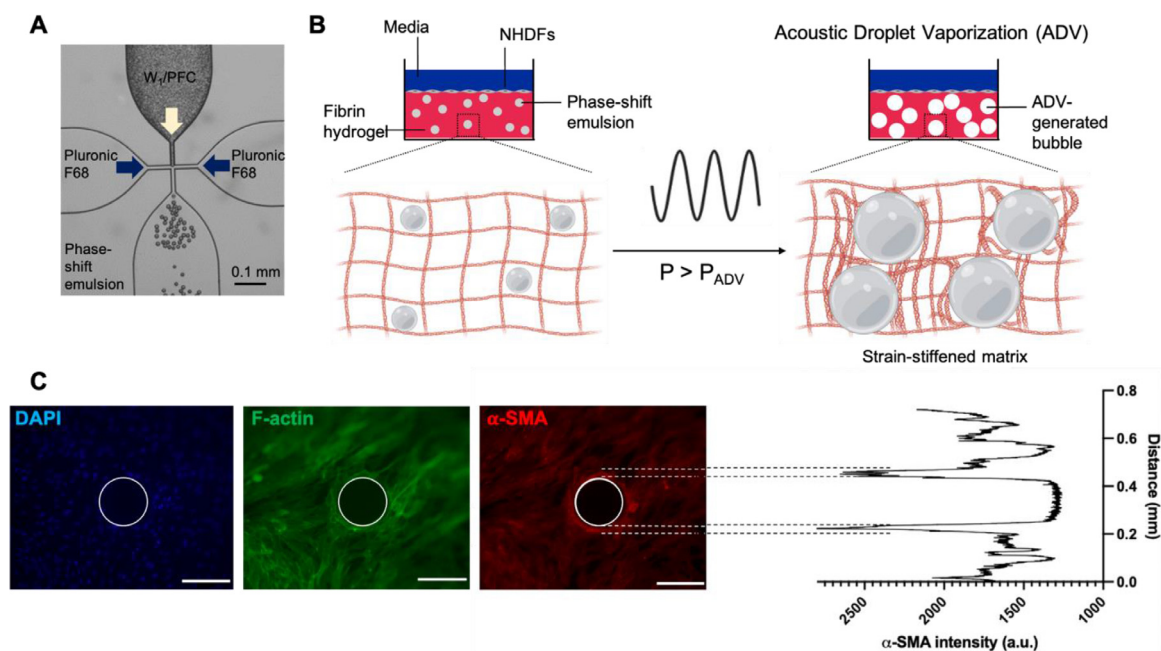


**Fig. 1.** An acoustically-responsive scaffold (ARS), which consists of a phase-shift emulsion embedded within a hydrogel matrix, enables local modulation of stiffness using focused ultrasound. (A) A microfluidic chip was used to create emulsion by encapsulating a perfluoroheptane core in Pluronic F-68 surfactant. (B) The emulsion vaporizes into a gas bubble when ultrasound with a pressure exceeding the acoustic droplet vaporization threshold (i.e.,  $P > P_{ADV}$ ) is applied to the ARS. The generated bubble and its subsequent expansion due to in-gassing compacts the surrounding fibrin matrix, which causes stiffening. Normal human dermal fibroblasts (NHDFs) were plated on top of fibrin-based ARSs containing monodispersed emulsions either before (i.e., *in situ*) or after (i.e., *ex situ*) ultrasound exposure. (C) Representative images of NHDFs stained for nuclei (blue), F-actin (green), and  $\alpha$ -SMA (red) on an ARS. The ultrasound-generated bubble is demarcated by a white circle (scale bars = 0.2 mm). The corresponding line plot of  $\alpha$ -SMA intensity shows elevated signal proximal to the bubble.

### 2.3. US exposure setup and parameters

ADV experiments were all conducted in a water tank (30 cm x 60 cm x 30 cm) filled with degassed, deionized water at 37°C. A calibrated, focused transducer (H108, 2.5 MHz, f-number = 0.83, radius of curvature = 50 mm, Sonic Concepts Inc., Bothell, WA, USA) was driven at its fundamental frequency to cause ADV within the ARS. The axial length and lateral width of the ultrasound focal volume, measured at full width half maximum with a fiber optic hydrophone, were  $3.9 \pm 0.1$  mm and  $0.7 \pm 0.1$  mm, respectively. Pulsed waveforms (peak rarefactional pressure: 6 MPa, pulse duration: 5.4  $\mu$ s; pulse repetition frequency: 100 Hz; duty cycle: 0.05%) were generated by a function generator (33500B, Agilent Technologies, Santa Clara, CA, USA) and amplified by a gated radiofrequency amplifier (GA-2500A Ritec Inc., Warwick, RI, USA). This peak rarefactional pressure was previously shown to be suprathreshold for ADV within the ARS containing C<sub>7</sub>F<sub>16</sub> emulsion [40]. The generated amplified signals were viewed and monitored in real-time on an oscilloscope (HDO4034, Teledyne LeCroy, Chestnut Ridge, NY, USA).

The transducer was connected to a three-axis positioning system controlled by MATLAB (The MathWorks, Natick, MA, USA) and localized axially with respect to the ARS using a pulse echo technique described previously [41]. During ultrasound exposure, the transducer was rastered at a speed of 5 mm/s with a 0.5 mm lateral spacing between raster lines. Exposures were done at three axial planes located 3 mm, 2 mm, and 1 mm above the well bottom, with exposures completed from the top/distal (i.e., 3 mm) to bottom/proximal (i.e., 1 mm) direction. The time required to complete the ultrasound exposure for each ARS was approximately 5 min.

### 2.4. Micromechanical characterization of acellular ARS

Force-distance curves were acquired 1h post-ADV on ARSs (h: ~1 mm) using the TT-atomic force microscope (AFM Workshop,

CA, USA). The samples were mechanically interrogated using a pre-calibrated probe (nominal spring constant: 0.064 N/m, Novascan, IA, USA) with a spherical glass bead (radius: 1  $\mu$ m). Atomic software (<http://sourceforge.net/projects/jrobust>) was used to convert force-distance curves into force-indentation curves. The compressive Young's modulus was approximated from the force-indentation curves using the Hertz model as described previously [20,42]. AFM measurements were performed in DMEM at room temperature.

### 2.5. Cell culture

Normal human dermal fibroblasts (NHDFs, single donor, Lonza, Walkersville, MD, USA) were cultured in complete media consisting of DMEM supplemented with 10% (v/v) fetal bovine serum (FBS, Corning, Glendale, AZ, USA), 100 U/mL penicillin, and 100  $\mu$ g/mL streptomycin. Media was exchanged every 2-3 days and cells were harvested below 80% confluence with trypsin-EDTA (Life Technologies). Experiments were conducted with cells between passages 3-5.

To investigate the impact of substrate stiffness on NHDF behavior, polydimethylsiloxane (PDMS) substrates ( $\mu$ -Dish ESS, 35 mm diameter, ibidi, Martinsreid, Germany) with Young's moduli of 1.5 kPa, 15 kPa, and 28 kPa were coated with fibrinogen [43]. Briefly, the substrates were overlaid with 1 mL of 0.8 mg/mL fibrinogen solution in 1 M Tris-HCl and incubated at 37°C for 2 h. Fibrinogen<sub>647</sub> was used to confirm that this procedure yielded equivalent binding of fibrinogen for the substrates with differing moduli. NHDFs were seeded onto the substrates at a density of 2,600 cells/cm<sup>2</sup> in complete media with or without 5 ng/mL TGF- $\beta$ 1 (Cat#: 7754-BH, R&D Systems, Minneapolis, MN, USA). Experiments were also performed with NHDFs plated in starvation media consisting of DMEM supplemented with 1% (v/v) FBS, 100 U/mL penicillin, and 100  $\mu$ g/mL streptomycin. Additionally, cells were seeded in 24-well tissue culture plastic plates (TCP, Costar, Corn-

**Table 1**  
A summary of the experimental conditions is shown.

Cell substrate	Ultrasound	Media	Culture	Exogenous TGF- $\beta$ 1	SB431542
PDMS + TCP	None	Complete	5 d	+/-	-
Fibrin	None	Complete	5 d	+/-	-
Fibrin	In situ	Complete	5 d	+/-	-
ARS	None	Complete	5 d	+/-	-
ARS	Ex situ	Complete	5 d	+/-	-
ARS	In situ	Complete	5 d	+/-	-
PDMS + TCP	None	Starvation	3 d	-	+/-
ARS	None	Starvation	3 d	-	+/-
ARS	Ex situ	Starvation	3 d	-	+/-
ARS	In situ	Starvation	3 d	-	+/-

ing) in both complete and starvation media. The media was exchanged every 2 days for all conditions. Cells were cultured for 5 days in complete media and 3 days in starvation media in a standard tissue culture incubator (37°C, 5% carbon dioxide). The experimental conditions for cell studies are summarized in Table 1.

For studies with ARSs, two different ultrasound exposure conditions were investigated. First, an *ex situ* exposure was conducted wherein the ARS was exposed to ultrasound to generate ADV. Subsequently, NHDFs were plated on top of the gels at 2,600 cells/cm<sup>2</sup>. Second, an *in situ* exposure was interrogated wherein NHDFs were plated on top of the ARS at 2,600 cells/cm<sup>2</sup> for 1 hr prior to ultrasound exposure. ARSs not exposed to ultrasound served as controls. Studies were conducted in complete media with or without 5 ng/mL TGF- $\beta$ 1. Additionally, studies were completed in starvation media with or without 10  $\mu$ M SB431542 (CAS# 301836-41-9, Tocris, Bristol, United Kingdom), an inhibitor of TGF- $\beta$ 1 receptor [44]. In all cases, the media was exchanged every 2 days. Unless otherwise noted, cells were cultured for 5 days in complete media and 3 days in starvation media. As additional controls, NHDFs were plated on fibrin-only gels, with the same fibrin density as the ARSs, and exposed to no ultrasound or *in situ* ultrasound.

## 2.6. Cell staining

Cells cultured on PDMS, TCP, fibrin gels, and ARSs were fixed in aqueous buffered zinc formalin (Z-Fix, Anatech, Battle Creek, MI, USA) and permeabilized with 0.1% (v/v) Triton-X100 (Sigma-Aldrich) in PBS. Triplicate washings with PBS were conducted between steps. Constructs were then incubated in a blocking solution containing 0.1% (v/v) Tween 20 (Sigma-Aldrich), 1% (w/v) bovine serum albumin, 10% (v/v) goat serum (Life Technologies), and 0.3 M glycine (Sigma-Aldrich) in PBS. Subsequently, constructs were stained overnight at 4°C with Alexa Fluor 555-labeled anti- $\alpha$ -SMA antibody (1:400 dilution, ab202509, abcam, Cambridge, MA, USA) and Alex Fluor 488-labeled phalloidin (1:400 dilution A12379, Molecular Probes). The following day, constructs were washed in triplicate and stained overnight with 1  $\mu$ g/mL 4,6'-diamidino-2-phenylindole (DAPI, Thermo Fisher Scientific, Waltham, MA, USA) in PBS. After triplicate washing, constructs were imaged.

We also interrogated whether *in situ* ultrasound exposure caused relatively immediate changes to NHDFs cultured on fibrin gels or ARSs. Cells were allowed to adhere for 1 hr prior to ultrasound exposure. Within 30 min of completing the exposure, the media overlying the constructs was replaced with fresh media and the constructs were stained with 16.2  $\mu$ M Hoechst 33342 (Molecular Probes) and 15  $\mu$ M propidium iodide (PI, Molecular Probes). Constructs were imaged soon after staining. Constructs that were not exposed to ultrasound served as controls.

## 2.7. Optical imaging and analysis

To study the ADV-induced microstructural changes in the matrix, acellular ARS (h  $\sim$ 3 mm) were imaged 1h post-ADV in a cell chamber (Attofluor, A7816, Thermo Fisher Scientific, Waltham, MA, USA) with a laser scanning confocal microscope (LSM800, Zeiss, Pleasanton, CA, USA) using a 40x objective. The laser power was set to the lowest non-zero setting (0.2%) to minimize saturation. Intensity measurements were performed on selected confocal images using ZEN lite software (Zeiss).

Cells and bubbles were imaged with an inverted microscope (Eclipse Ti-E, Nikon, Melville, NY, USA) with a 10x objective lens and acquisition software (MetaMorph, Molecular Devices, San Jose, CA, USA). Cell density was quantified based on DAPI or Hoechst staining. The fraction of dead cells and/or cells with permeabilized membranes was determined based on PI staining. For each field of view, a stack of  $\alpha$ -SMA images was acquired using a 1 s exposure time per image and then converted to a maximum intensity projection image for subsequent analysis. Images were analyzed in ImageJ (National Institutes of Health, Bethesda, MD, USA) by thresholding the cells based on the  $\alpha$ -SMA signal and then computing the average intensity of the cells. For ARS, cells were analyzed in regions proximal and distal to the ADV-generated bubbles, which were defined as regions within 0.1 mm and greater than 0.5 mm from the bubble, respectively. These regions were defined based on considering the width of fibrin compaction observed in a prior study [20] and the dimensions of the NHDFs in 2D.

## 2.8. Statistics

Statistical analyses were performed using GraphPad Prism software (GraphPad Software, Inc., La Jolla, CA, USA). The number of independent replicates is listed in the caption for each figure. Significant differences between groups were determined using a one-way ANOVA followed by Tukey's multiple comparisons test. A significance level of 0.05 was used.

## 3. Results

### 3.1. Microstructural and micromechanical characterization of ARSs post-ADV

Prior to ADV, the fibrin network surrounding the phase-shift emulsion droplet ( $\emptyset$ :  $\sim$ 13.5  $\mu$ m), which appears dark, was visible within the ARS (Fig. 2A). The droplet was converted into a bubble ( $\emptyset$ :  $\sim$ 200  $\mu$ m) by ADV, thereby consolidating the fibrin matrix surrounding the bubble and increasing the fluorescence signal within the matrix (Fig. 2B, C).

The elevated fibrinogen<sub>647</sub> intensity at the bubble-fibrin interface, due to the ADV-induced mechanical strain, can be seen in regions proximal to the ADV-bubble (Fig. 2D). The corresponding

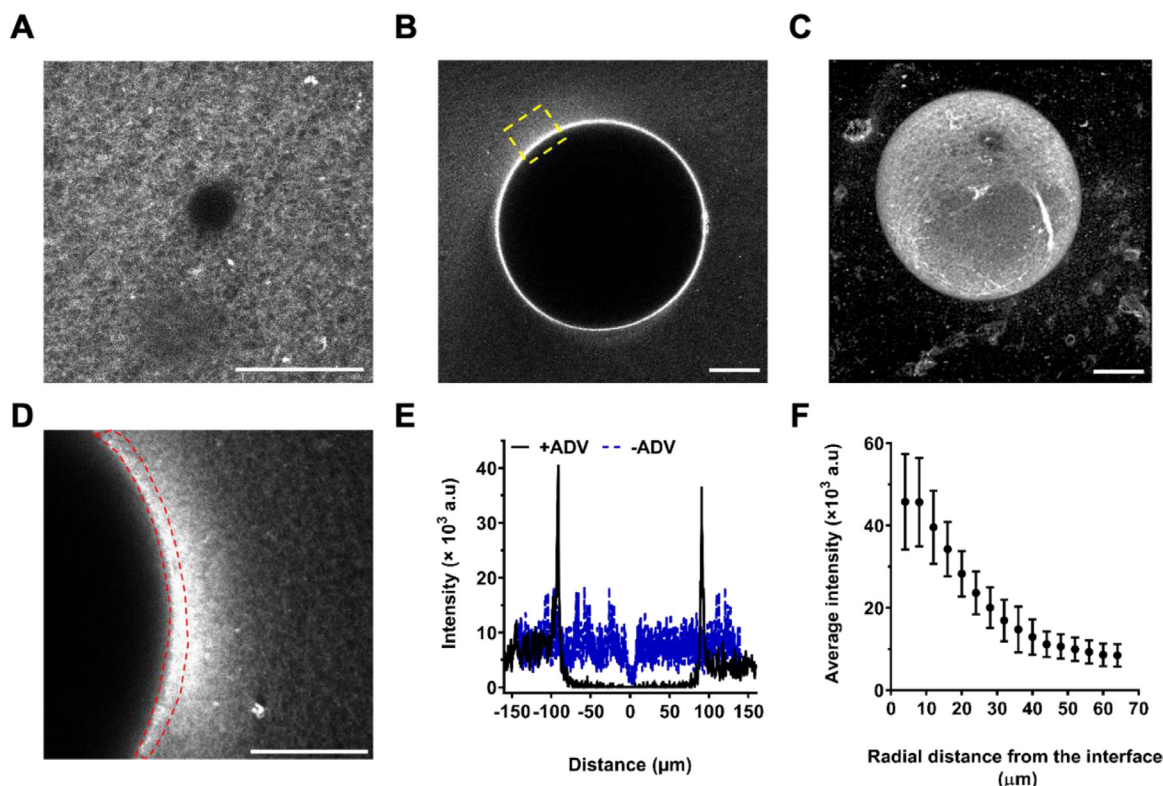


**Fig. 2.** Acoustic droplet vaporization (ADV) resulted in local, radial compaction of fibrin surrounding the bubbles. Confocal microscopy images of acoustically-responsive scaffolds (ARSs) before (A) and 1-hour after (B) ADV. The fibrin matrix contained Alexa Fluor 647-labeled fibrinogen (fibrinogen<sub>647</sub>). C) Maximum intensity projection confocal image of an ADV-generated bubble in an ARS. The region of interest (ROI) outlined in yellow dashed lines in (B) is enlarged in (D) and indicates significantly higher fibrinogen<sub>647</sub> intensity at the bubble-matrix interface. E) Line intensity measurements of fibrinogen<sub>647</sub> before and 1-hour after ADV are shown. The average intensity of fibrinogen<sub>647</sub> as a function of distance from the bubble interface (F) was computed by segmenting the matrix into ROIs, each having a length of 4  $\mu\text{m}$ . The ROI most proximal to the bubble interface is outlined with red dashed lines in (D). Scale bar: 30  $\mu\text{m}$ .

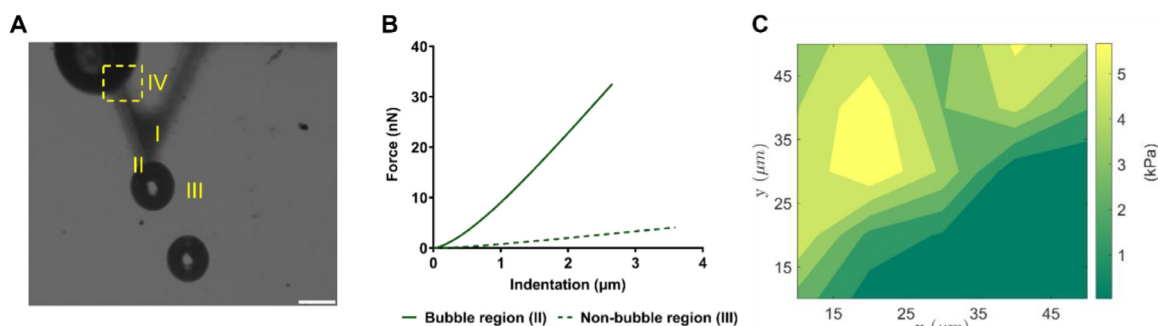


**Fig. 3.** Atomic force microscopy was used to characterize micromechanical properties of acoustically-responsive scaffolds (ARSs) after acoustic droplet vaporization (ADV). A) An optical image of an ARS post-ADV shows four regions defined as: cantilever with a 2  $\mu\text{m}$  glass bead (I), region proximal to the ADV-bubble (II), region distal to the ADV-bubble (III), and a 50  $\mu\text{m} \times 50 \mu\text{m}$  area selected for indentation mapping (IV). B) A comparison of force-indentation responses in regions II & III, indicates a significant difference in stiffness. C) The Young's modulus was mapped in region IV. Scale bar: 100  $\mu\text{m}$ .

line intensity profiles of Fig. 2A and B are shown (Fig. 2E), indicating locally enhanced fibrinogen intensity and formation of denser regions at the bubble-fibrin interface. To quantify the microstructural changes, the confocal image in Fig. 2D was segmented into 16 regions of interest (ROIs), each having a length of  $\sim 4 \mu\text{m}$ . The average fibrinogen intensity decreased exponentially from the ROI proximal to the bubble to the most distal (Fig. 2F).

ADV-induced micromechanical changes in ARSs were characterized using AFM. Typical force indentation responses in regions proximal (shown as region II in Fig. 3A) and distal (shown as region III in Fig. 3A) to the ADV-bubble are shown (Fig. 3B). To assess the spatial variation in Young's moduli, the moduli were mapped in a 50  $\mu\text{m} \times 50 \mu\text{m}$  area (shown as IV in Fig. 3A) adjacent to a bubble in an ARS (Fig. 3C). The lowest and the highest measured

Young's moduli in this area were 0.23 kPa and 6.7 kPa, respectively. Thus, ADV generated highly localized increases in moduli.

### 3.2. Cell density and $\alpha$ -SMA expression on PDMS and TCP substrates with complete media

Representative images of  $\alpha$ -SMA-stained NHDFs cultured on fibrinogen-coated PDMS substrates and TCP, with and without TGF- $\beta$ 1, are shown (Fig. 4A). In general, cell density (Fig. 4B) correlated with substrate stiffness and the addition of TGF- $\beta$ 1. For all substrates, addition of TGF- $\beta$ 1 yielded significantly greater cell density compared to the corresponding control condition without TGF- $\beta$ 1. A significantly higher cell density was seen on 28 kPa PDMS and TCP substrates compared to 1.5 kPa and 15 kPa PDMS substrates.

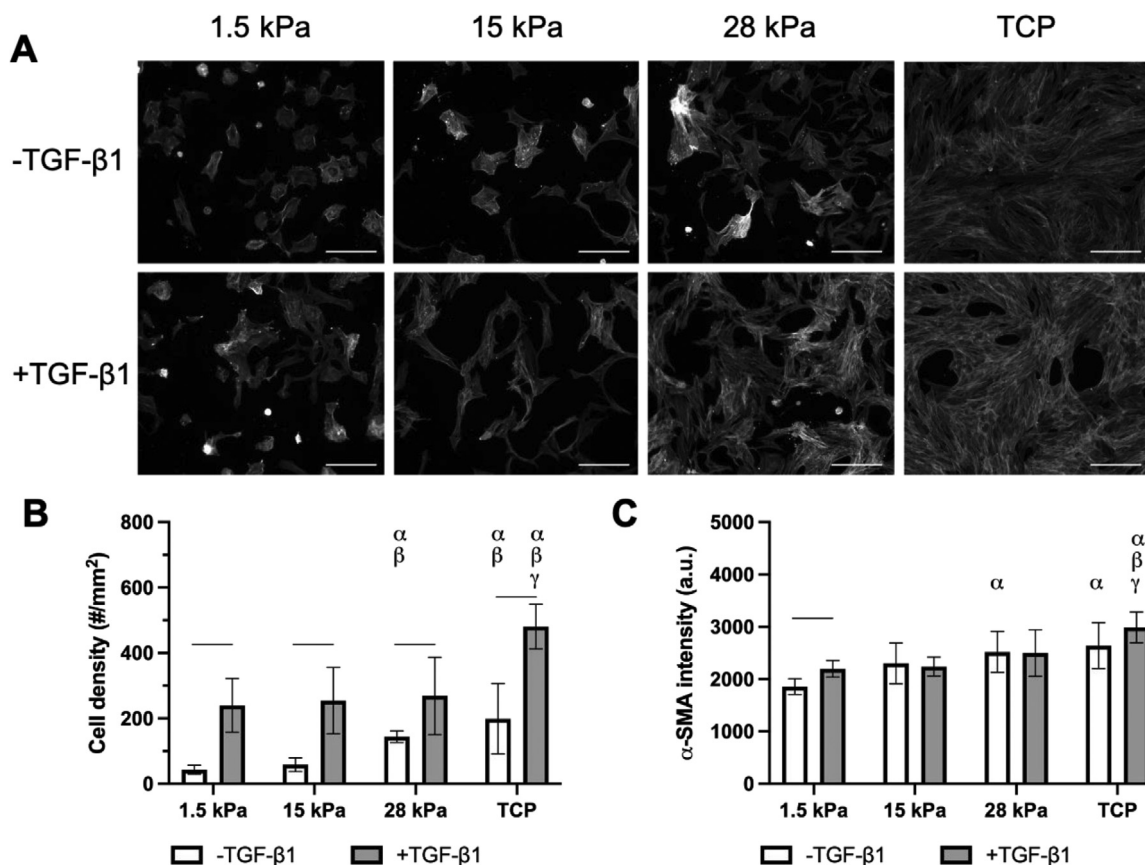


**Fig. 4.** Cell density and  $\alpha$ -SMA expression in NHDFs were dependent on substrate stiffness and the presence of exogenous TGF- $\beta$ 1. A) Fluorescence images of NHDFs, which were stained for  $\alpha$ -SMA, cultured on fibrinogen-coated PDMS substrates with different Young's moduli and tissue culture plastic (TCP). Cells were cultured for 5 days in complete media with or without 5 ng/mL TGF- $\beta$ 1. Scale bar = 0.25 mm. B) Cell density was quantified based on DAPI staining. C) The level of  $\alpha$ -SMA expression was quantified based on immunocytochemical staining. All data are represented as mean  $\pm$  standard deviation (N = 3 plates per group with 3–5 fields of view per construct). Statistically significant differences ( $p < 0.05$ ) between the same TGF- $\beta$ 1 conditions are denoted as follows:  $\alpha$  vs. 1.5 kPa,  $\beta$  vs. 15 kPa, and  $\gamma$  vs. 28 kPa. A horizontal bar shows pairwise differences among +/- TGF- $\beta$ 1 conditions.

$\alpha$ -SMA expression of NHDF cells was enhanced as stiffness of the PDMS substrates increased (Fig. 4C). A significant increase in  $\alpha$ -SMA expression was noted between the 1.5 kPa and 28 kPa PDMS substrates ( $p = 0.007$ ), as well as between the 1.5 kPa substrate and TCP ( $p < 0.001$ ). Interestingly, only the 1.5 kPa condition was significantly affected by the addition of exogenous TGF- $\beta$ 1 ( $p < 0.001$ ).

### 3.3. Cell density and $\alpha$ -SMA expression on ARSs in complete media

NHDFs were seeded onto fibrin-based ARSs either immediately after ultrasound exposure (i.e., *ex situ* exposure) or one hour before exposure (i.e., *in situ* exposure) and cultured for 5 days in complete media. Representative  $\alpha$ -SMA images for each exposure condition are shown (Fig. 5A). Cell density decreased when ultrasound was applied *in situ* compared to no ultrasound or *ex situ* exposures (Fig. 5B). When cells seeded onto ARSs or fibrin gels were stained immediately after *in situ* ultrasound, no differences in cell density were observed when comparing *in situ* ultrasound versus no ultrasound conditions (Supplemental Fig. 1A). Additionally, the fraction of PI<sup>+</sup> cells adhered to the ARS was not significantly impacted by *in situ* ultrasound.

In the absence of ultrasound (Fig. 5C),  $\alpha$ -SMA levels of NHDFs on ARSs increased when the overlying media was supplemented with 5 ng/mL TGF- $\beta$ 1 ( $p = 0.047$ ). For all conditions with ultrasound exposure, irrespective of the addition of exogenous TGF- $\beta$ 1, expression of  $\alpha$ -SMA proximal to the ADV-generated bubble was significantly higher than in regions distal to the ADV-generated

bubble (Fig. 5D and E). With *ex situ* exposure (Fig. 5D), the differences between proximal and distal regions for +TGF- $\beta$ 1 ( $p < 0.001$ ) and -TGF- $\beta$ 1 ( $p < 0.001$ ) conditions were significant. With *in situ* exposure (Fig. 5E), the differences between proximal and distal regions for +TGF- $\beta$ 1 ( $p = 0.004$ ) and -TGF- $\beta$ 1 ( $p = 0.03$ ) conditions were also significant. *In situ* ultrasound also increased the overall expression of  $\alpha$ -SMA across both +/- TGF- $\beta$ 1 conditions compared to the *ex situ* counterparts. For NHDFs cultured on fibrin gels, *in situ* ultrasound did not cause an increase in  $\alpha$ -SMA, regardless of the addition of exogenous TGF- $\beta$ 1 (Supplemental Fig. 2). However,  $\alpha$ -SMA increased significantly with the addition of exogenous TGF- $\beta$ 1 to fibrin gels ( $p < 0.001$ ) for both no ultrasound and *in situ* ultrasound). The sizes of bubbles in ARSs generated by ADV were not significantly different when comparing *ex situ* versus *in situ* ultrasound (Supplemental Fig. 3A).

### 3.4. Cell density and $\alpha$ -SMA expression on PDMS and TCP substrates in starvation media

Representative images of  $\alpha$ -SMA-stained NHDFs cultured on fibrinogen-coated PDMS substrates and TCP in starvation media without addition of exogenous TGF- $\beta$ 1 are shown (Fig. 6A). Unlike the complete media conditions, cell densities did not significantly increase as matrix stiffness incremented (Fig. 6B). Additionally, cell density was significantly lower in starvation conditions compared to complete media conditions. There was no correlation between substrate stiffness and  $\alpha$ -SMA expression (Fig. 6C), though levels

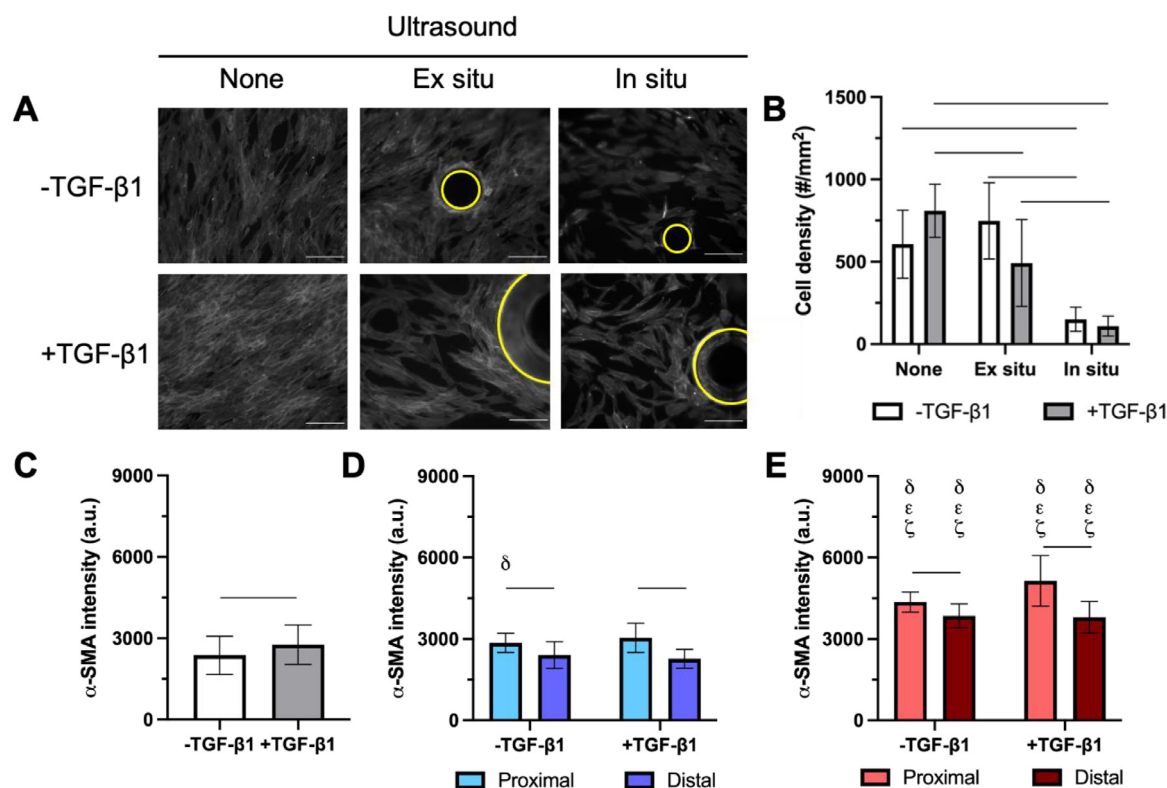


**Fig. 5.**  $\alpha$ -SMA was elevated in NHDFs proximal to bubbles generated by acoustic droplet vaporization (ADV) compared to distal cells. A) Fluorescence images of NHDFs, which were stained for  $\alpha$ -SMA, cultured on fibrin-based ARSs. Cells were plated on ARSs after exposure to ultrasound (i.e., *ex situ* exposure) or prior to exposure to ultrasound (i.e., *in situ* exposure, which generated ADV). Constructs were cultured for 5 days in complete media with or without 5 ng/mL TGF- $\beta$ 1. Bubbles, denoted by yellow circles, are observed in +ultrasound groups. Scale bar = 0.25 mm. B) Cell density was quantified based on DAPI staining. The level of  $\alpha$ -SMA expression was quantified based on immunocytochemical staining for C) no ultrasound exposure, D) +ultrasound (*ex situ* exposure), and E) +ultrasound (*in situ* exposure) conditions. All data are represented as mean  $\pm$  standard deviation (N = 3–5 ARSs per group with 3–5 fields of view per construct). For +ultrasound groups, cells were analyzed in regions proximal and distal to the bubbles, which are defined as regions within 0.1 mm and greater than 0.5 mm from the bubble edge, respectively. Statistically significant differences ( $p < 0.05$ ) between the same TGF- $\beta$ 1 conditions are denoted as follows:  $\delta$  vs. -ultrasound condition,  $\varepsilon$  vs. +ultrasound (*ex situ* exposure, proximal region), and  $\zeta$  vs. +ultrasound (*ex situ* exposure, distal region). A horizontal bar shows pairwise differences.

were significantly elevated relative to corresponding complete media conditions with +/- TGF- $\beta$ 1 (Fig. 4C).

### 3.5. Cell density and $\alpha$ -SMA expression on ARSs in starvation media

NHDFs were seeded onto fibrin-based ARSs and cultured for 3 days in starvation media. Representative  $\alpha$ -SMA images for each exposure condition are shown (Fig. 7A). There was a trend for cell density to decrease when ultrasound was applied *ex situ* and *in situ* compared to no ultrasound exposure (Fig. 7B). The addition of SB431542 yielded significant decreases in cell density for *ex situ* ( $p = 0.005$ ) and *in situ* ( $p = 0.03$ ) ultrasound. When cells seeded onto ARSs or fibrin gels were stained immediately after *in situ* ultrasound, no differences in cell density were observed when comparing *in situ* ultrasound versus no ultrasound conditions (Supplemental Fig. 1B). Additionally, the fraction of PI+ cells adhered to the ARS was not significantly impacted by *in situ* ultrasound. Compared to similar experiments in complete media (Supplemental Fig. 1A), significant decreases in cell density and increases in the fraction of PI+ cells were observed in starvation media.

In the absence of ultrasound (Fig. 7C), the addition of SB431542 caused a significant decrease in  $\alpha$ -SMA levels of NHDFs on ARSs ( $p = 0.01$ ). As observed in complete media, there was also an increase ( $p = 0.003$ ) in  $\alpha$ -SMA intensity proximal to ADV-generated bubbles compared to distal regions for the *ex situ* ultrasound exposure in the absence of SB431542 (i.e., vehicle) (Fig. 7D). However, with the addition of SB431542, there was no significant difference between proximal and distal  $\alpha$ -SMA levels. Similarly, with *in situ*

exposure in the presence of SB431542 (Fig. 7E), there was no significant difference between proximal and distal regions. In the absence of SB431542, there was a significant increase in  $\alpha$ -SMA when comparing proximal and distal regions ( $p = 0.004$ ). With ARSs, the sizes of bubbles generated by ADV were not significantly different when comparing *ex situ* versus *in situ* ultrasound (Supplemental Fig. 3B).

## 4. Discussion

Myofibroblasts play a key role in the repair of connective tissues like skin, bone, and cartilage. However, dysregulation of myofibroblasts can contribute to varied pathologies such as chronic wounds and fibrosis [26]. Elucidating the impact of spatiotemporally-regulated biochemical and biophysical cues on myofibroblast differentiation could assist with understanding disease progression and with the development of therapeutic interventions. Previously, normal human lung fibroblasts (NHLFs) cultured in 2D on collagen-coated polyacrylamide gels exhibited similar  $\alpha$ -SMA levels on gels with Young's moduli of 0.5 kPa and 2 kPa, but significantly elevated levels at 20 kPa [25]. Cell proliferation and  $\alpha$ -SMA levels of NHLFs correlated with the Young's moduli of protease-sensitive, dextran-based hydrogels in the range of 0.6 kPa to 6.1 kPa [45]. A similar correlation with  $\alpha$ -SMA was observed with portal fibroblasts cultured on collagen-coated polyacrylamide gels in the range of 0.4 kPa to 12 kPa [46]. Furthermore, addition of exogenous TGF- $\beta$ 1 caused upregulation of  $\alpha$ -SMA in human gingival fibroblasts grown on TCP [47]. Our study exhibits

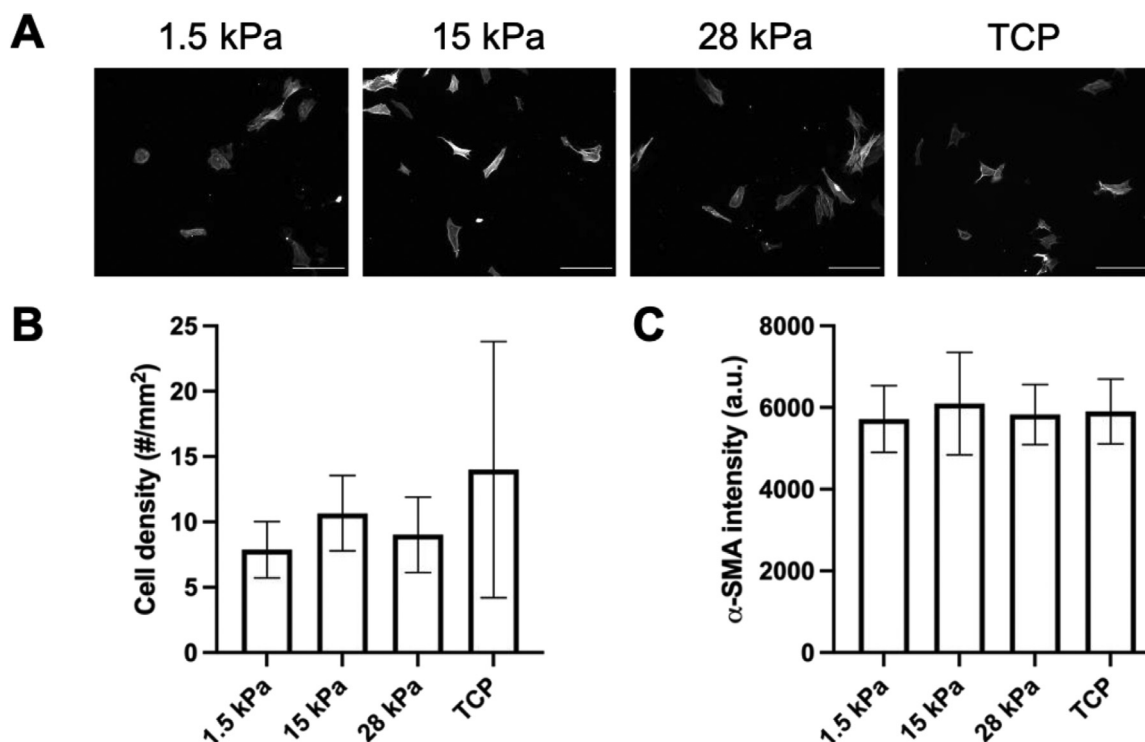


**Fig. 6.**  $\alpha$ -SMA levels increased in NHDFs cultured in low serum media compared to complete media. A) Fluorescent images of NHDFs, which were stained for  $\alpha$ -SMA, cultured on fibrinogen-coated PDMS substrates with different Young's moduli and tissue culture plastic (TCP). Cells were cultured for 3 days in starvation media. Scale bar = 0.25 mm. B) Cell density was determined based on DAPI staining. C) The level of  $\alpha$ -SMA expression was quantified based on immunocytochemical staining. All data are represented as mean  $\pm$  standard deviation (N = 3 plates per group with 3–5 fields of view per construct).

similar trends when NHDFs were cultured in complete media on fibrinogen-coated PDMS substrates and TCP.

In this study, *in situ* ultrasound did not elevate  $\alpha$ -SMA levels of NHDFs plated on fibrin-only scaffolds. It is important to note that in fibrin-only scaffolds, ADV is not generated due to the absence of phase-shift emulsion. In contrast, NHDFs consistently displayed higher levels of  $\alpha$ -SMA in regions proximal to an ADV-generated bubble compared to cells in distal regions when cultured in complete media and in starvation media without SB431542. This was attributed to the stiffening of the matrix surrounding the bubble, which was confirmed using atomic force microscopy. Within a 50  $\mu$ m x 50  $\mu$ m area in the ARS, there was a 29-fold increase in the Young's modulus 1-hour post-ADV when comparing proximal and distal regions. Thus, ADV-induced stiffening of the matrix was hyperlocal with respect to the generated bubble. Previously we showed that the intensity as well as the full width half maximum of the hyperlocal region increased significantly over time, as a result of bubble growth, reaching a 20-fold increase in Young's modulus on day 4 [20]. In complete media, the increase in  $\alpha$ -SMA in proximal regions was seen irrespective of the addition of exogenous TGF- $\beta$ 1. This could suggest involvement of autocrine TGF- $\beta$ 1 signaling based on deposition of latent TGF- $\beta$ 1 [48,49].  $\alpha$ -SMA levels increased when cells were cultured in starvation (i.e., low serum) media, which has been observed previously with differentiation of cardiac fibroblasts [50].

For NHDFs cultured in complete media, exposure to *in situ* ultrasound caused a significant increase in  $\alpha$ -SMA compared to *ex situ* ultrasound. This could be a result of the interaction of ultrasound with the NHDFs, specifically the generation of mechanical forces that can induce myofibroblast differentiation [51]. In skin fibroblasts, low intensity pulsed ultrasound (1.5 MHz, 0.2 ms pulse duration, 1 kHz pulse repetition frequency, 0.03 W/cm<sup>2</sup>, 11 min exposure) caused polymerization of F-actin and recruitment of pax-

illin to focal adhesions via activation of Rho kinase [52]. Following a 10 min exposure to low intensity pulsed ultrasound (3 MHz, 20% duty cycle, 0.1 W/cm<sup>2</sup> spatial average temporal peak), NHDFs cultured on TCP exhibited increased levels of  $\alpha$ -SMA and TGF- $\beta$ 1 after 24 h compared to non-exposed controls [53].

After culturing the ARSs for 5 days in complete media or 3 days in starvation media, groups exposed to ultrasound exhibited lower cell densities than corresponding groups without ultrasound exposure. This decrease was more evident for *in situ* exposure than for *ex situ* exposure. However, cell density and the fraction of PI+ cells on ARSs immediately after *in situ* exposure was not significantly different than ARSs not exposed to ultrasound. Ultrasound-induced cavitation of microbubbles [54,55] as well as ADV and subsequent acoustic cavitation [56,57] can increase cell membrane permeability for drug delivery (i.e., sonoporation) while also potentially impacting viability under certain conditions. PI, an indicator of cell death, is often used as a marker of sonoporation since it is impermeant to cells with intact membranes. Thus, the acoustic conditions used in this study did not increase membrane permeability and/or cell death. Therefore, *in situ* exposure could be impacting other cellular processes such as the rate of cell proliferation or migration. With *ex situ* exposure, cells were plated onto the ARS after the ultrasound exposure. Therefore, any impacts on cell density or behavior were not attributed to the direct interaction of the ultrasound and cells. Topographical changes to the surface of the ARS, which were induced by ADV, could have reduced the adherence of NHDFs when compared to ARSs without ultrasound exposure. The adhesion of human dermal foreskin fibroblasts decreased on cellulose substrates containing micron-sized pits (diameter: 3–20  $\mu$ m; spacing: 6–23  $\mu$ m) compared to identical flat substrates [58]. Human mesenchymal cells grown on concave surfaces of poly(trimethylene carbonate) exhibited less contact area and increased migration speed compared to cells on flat surfaces; com-

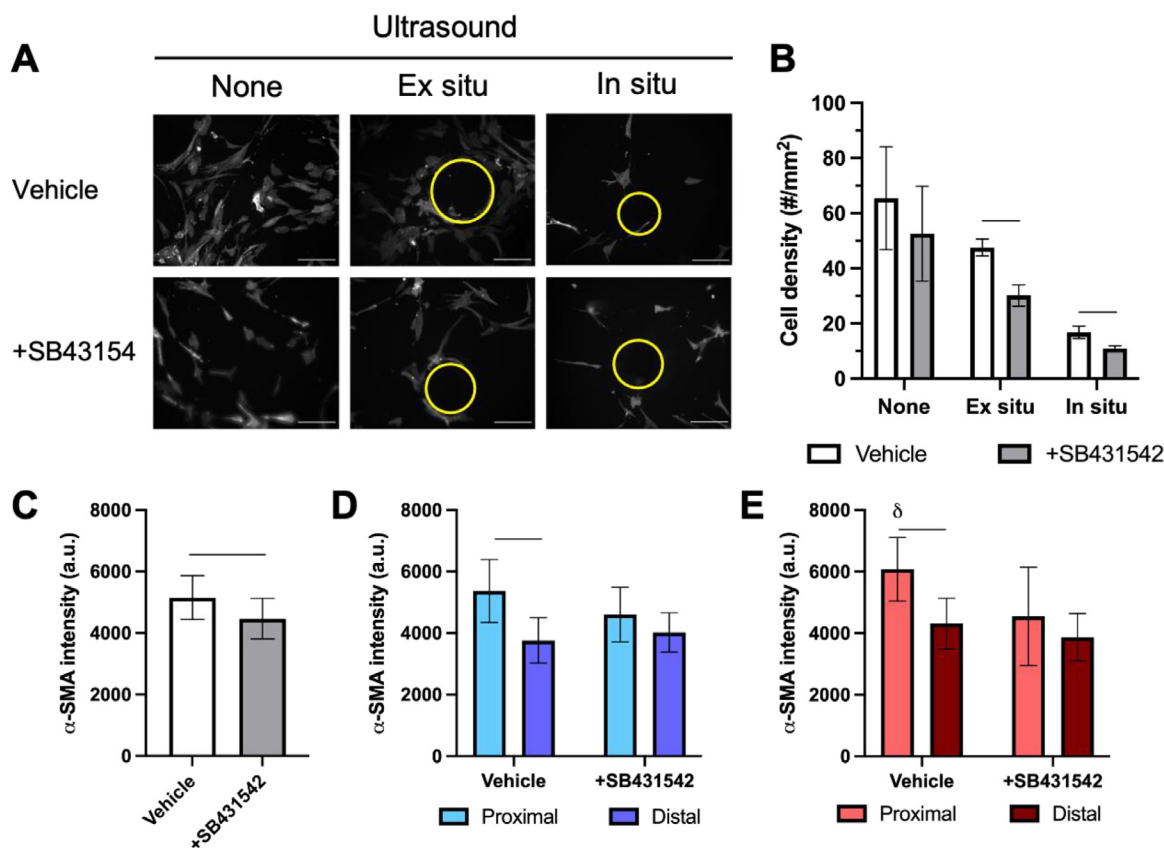


**Fig. 7.** Inhibition of TGF- $\beta$ 1 receptor abrogated the increase in  $\alpha$ -SMA levels observed proximal to bubbles generated by acoustic droplet vaporization (ADV). A) Fluorescence images of NHDFs, which were stained for  $\alpha$ -SMA, cultured on fibrin-based acoustically-responsive scaffolds (ARSS). Cells were plated on ARSS after exposure to ultrasound (i.e., *ex situ* exposure) or prior to exposure to ultrasound (i.e., *in situ* exposure) to generate ADV. Constructs were cultured for 3 days in starvation media with or without 10  $\mu$ M SB431542, an inhibitor of TGF- $\beta$ 1 receptor. Bubbles, denoted by yellow circles, are observed in +ultrasound groups. Scale bar = 0.25 mm. B) Cell density was determined by DAPI staining. The level of  $\alpha$ -SMA expression was quantified based on immunocytochemical staining for C) no ultrasound exposure, D) +ultrasound (*ex situ* exposure), and E) +ultrasound (*in situ* exposure) conditions. All data are represented as mean  $\pm$  standard deviation (N = 3–5 ARSS per group with 3–5 fields of view per construct). For +ultrasound groups, cells were analyzed in regions proximal and distal to the bubbles, which are defined as regions within 0.1 mm and greater than 0.5 mm from the bubble edge, respectively. A horizontal bar shows statistically significant differences ( $p < 0.05$ ) between pairs.

paratively, cells on convex surfaces displayed greater nuclear deformation, increased levels of lamin-A, and greater osteogenic differentiation [59]. Tensile forces can also increase the transition of fibroblasts to myofibroblasts [60].

The addition of SB431542, an inhibitor of TGF- $\beta$ 1 receptor, to starvation media decreased  $\alpha$ -SMA levels in the absence of ultrasound exposure and abrogated the elevated  $\alpha$ -SMA levels in proximal versus distal regions for both *ex situ* and *in situ* ultrasound exposures. These findings reveal that while TGF- $\beta$ 1 is necessary for establishing myofibroblast phenotype, exogenous TGF- $\beta$ 1 is not needed; instead, endogenous TGF- $\beta$ 1 production induced by matrix stiffness is sufficient for prompting differentiation.

There were some limitations to this study. First, myofibroblast differentiation was studied in 2D rather than 3D, which would more closely mimic the microenvironment of a chronic wound or fibrotic tissue. Interestingly, differentiation in 3D was shown to correlate inversely with Young's modulus in synthetic matrices [45]. Second, studies were conducted with fibrinogen-coated PDMS substrates and fibrin-based ARSS. Collagen, which also exhibits strain stiffening behavior [61], has been used in other studies of myofibroblast differentiation [62]. Thus, the impact of matrix chemistry and architecture warrants further investigation. Third, ADV-generated bubbles altered other parameters (e.g., ligand density, bubble-mediated curvature) in addition to matrix stiffness that could impact myofibroblast differentiation. Fourth, the growth of a bubble generated by ADV consists of two phases:

the ultrasound-mediated conversion of liquid PFC into PFC vapor [63] and the subsequent growth of the bubble as it equilibrates with the local microenvironment [15]. The former occurs much more rapidly than the latter. The relative contributions of each phase to myofibroblast differentiation remains unexplored. Fifth, ADV-induced mechanical changes to the ARS were studied in the absence of ADV-triggered payload delivery. However, the combined stiffening of the matrix along with release of a relevant payload (e.g., TGF- $\beta$ 1) could enable the simultaneous study of spatiotemporally-modulated biophysical and biochemical cues, which would be important in more closely recapitulating disease models.

Future studies investigating how properties of the emulsion, hydrogel matrix, and ultrasound impact matrix stiffening as well as induced biological responses are warranted. For example, in addition to  $\alpha$ -SMA, myofibroblasts also exhibit increased secretion of collagen [64] and fibronectin [65]. Overall, the demonstration that dynamically changing mechanical cues in an ARS alter fibroblast behavior could be used in developing models of fibrosis and for therapeutic applications. Ultrasound can penetrate tissue and generate ADV within implanted ARSS [22]. Thus, this technique is amenable of impacting not only cells that are encapsulated within the ARS but also host cells that migrate into the ARS [23,24]. By using focused ultrasound, as done in this study, ADV can be generated within sub-volumes of an ARS, thereby enabling the generation of spatially patterned heterogeneities to influence cell behav-

ior. Additionally, ADV-generated bubbles can be detected acoustically using B-mode imaging as well as non-imaging techniques like active and/or passive detection [66], which could facilitate mapping of myofibroblast differentiation within an ARS.

## 5. Conclusions

Ultrasound was used to locally stiffen the fibrin matrix surrounding bubbles generated within an ARS. This radial stiffening, caused by the increase in particle size as the phase-shift emulsion was acoustically converted from a liquid droplet into a gas bubble, caused consolidation of the strain-stiffening fibrin matrix. NHDFs proximal to these stiffened matrix regions displayed higher levels of  $\alpha$ -SMA expression compared to distal regions. This increase in  $\alpha$ -SMA occurred irrespective of the addition of exogenous TGF- $\beta$ 1, thereby suggesting that endogenous production of TGF- $\beta$ 1 was sufficient for the induction of myofibroblast phenotype.

## Declaration of Competing Interest

The authors declare that they have no known competing financial interests or personal relationships that could have appeared to influence the work reported in this paper.

## Acknowledgments

This work was supported by NIH Grant R01HL139656 (M.L.F.). Special thanks to Dr. Allen Brooks (Department of Radiology) for assisting with the synthesis of the fluorosurfactant, Aniket Jivani (Department of Radiology) for designing the holder for the ultrasound transducer, and Dr. William Weadock (Department of Radiology) for helping with 3D printing of CAD designs. The authors also wish to thank the Single Molecule Analysis in Real-Time (SMART) Center of the University of Michigan, seeded by NSF MRI-R2-ID award DBI-0959823 to Nils G. Walter, as well as Dr. J. Damon Hoff for training, technical advice and use of TT-AFM.

## Supplementary materials

Supplementary material associated with this article can be found, in the online version, at [doi:10.1016/j.actbio.2021.11.020](https://doi.org/10.1016/j.actbio.2021.11.020).

## References

- [1] A.J. Engler, S. Sen, H.L. Sweeney, D.E. Discher, Matrix elasticity directs stem cell lineage specification, *Cell* 126 (4) (2006) 677–689.
- [2] N. Huebsch, P.R. Arany, A.S. Mao, D. Shvartsman, O.A. Ali, S.A. Bencherif, J. Rivera-Feliciano, D.J. Mooney, Harnessing traction-mediated manipulation of the cell/matrix interface to control stem-cell fate, *Nat. Mater.* 9 (6) (2010) 518–526.
- [3] S. Khetan, M. Guvendiren, W.R. Legant, D.M. Cohen, C.S. Chen, J.A. Burdick, Degradation-mediated cellular traction directs stem cell fate in covalently crosslinked three-dimensional hydrogels, *Nat. Mater.* 12 (5) (2013) 458–465.
- [4] T. Ebata, Y. Mitsui, W. Sugimoto, M. Maeda, K. Araki, H. Machiyama, I. Harada, Y. Sawada, H. Fujita, H. Hirata, K. Kawauchi, Substrate stiffness influences doxorubicin-induced p53 activation via ROCK2 expression, *Biomed. Res. Int.* 2017 (2017) 5158961.
- [5] W.W. Xu, R. Mezenцев, B. Kim, L.J. Wang, J. McDonald, T. Sulchek, Cell stiffness is a biomarker of the metastatic potential of ovarian cancer cells, *PLoS One* 7 (10) (2012).
- [6] T.J. Keane, C.M. Horejs, M.M. Stevens, Scarring vs. functional healing: matrix-based strategies to regulate tissue repair, *Adv. Drug. Deliv. Rev.* 129 (2018) 407–419.
- [7] S.R. Cialiari, J.A. Burdick, A practical guide to hydrogels for cell culture, *Nat. Methods* 13 (5) (2016) 405–414.
- [8] M. Liu, X. Zeng, C. Ma, H. Yi, Z. Ali, X. Mou, S. Li, Y. Deng, N. He, Injectable hydrogels for cartilage and bone tissue engineering, *Bone Res.* 5 (2017) 17014.
- [9] M.V. Monteiro, V.M. Gaspar, L.P. Ferreira, J.F. Mano, Hydrogel 3D in vitro tumor models for screening cell aggregation mediated drug response, *Biomater. Sci.* 8 (7) (2020) 1855–1864.
- [10] J. Leijten, J. Seo, K. Yue, G.T. Santiago, A. Tamayol, G.U. Ruiz-Esparza, S.R. Shin, R. Sharifi, I. Noshadi, M.M. Alvarez, Y.S. Zhang, A. Khademhosseini, Spatially and temporally controlled hydrogels for tissue engineering, *Mater. Sci. Eng. R. Rep.* 119 (2017) 1–35.
- [11] J.A. Burdick, W.L. Murphy, Moving from static to dynamic complexity in hydrogel design, *Nat. Commun.* 3 (2012) 1269.
- [12] R.A. Marklein, J.A. Burdick, Spatially controlled hydrogel mechanics to modulate stem cell interactions, *Soft Matter* 6 (1) (2010) 136–143.
- [13] C. Yang, F.W. DelRio, H. Ma, A.R. Killars, L.P. Basta, K.A. Kyburz, K.S. Anseth, Spatially patterned matrix elasticity directs stem cell fate, *PNAS* 113 (31) (2016) E4439–E4445.
- [14] A. Moncion, K.J. Arlotta, O.D. Kripfgans, J.B. Fowlkes, P.L. Carson, A.J. Putnam, R.T. Franceschi, M.L. Fabiilli, Design and characterization of fibrin-based acoustically responsive scaffolds for tissue engineering applications, *Ultrasound Med. Biol.* 42 (1) (2016) 257–271.
- [15] O.D. Kripfgans, J.B. Fowlkes, D.L. Miller, O.P. Eldevik, P.L. Carson, Acoustic droplet vaporization for therapeutic and diagnostic applications, *Ultrasound Med. Biol.* 26 (7) (2000) 1177–1189.
- [16] M.L. Fabiilli, K.J. Haworth, N.H. Fakhri, O.D. Kripfgans, P.L. Carson, J.B. Fowlkes, The role of inertial cavitation in acoustic droplet vaporization, *IEEE Trans. Ultrason. Ferroelectr. Freq. Control* 56 (5) (2009) 1006–1017.
- [17] O. Shpak, M. Verweij, H.J. Vos, N. de Jong, D. Lohse, M. Versluis, Acoustic droplet vaporization is initiated by superharmonic focusing, *PNAS* 111 (5) (2014) 1697–1702.
- [18] D.S. Li, O.D. Kripfgans, M.L. Fabiilli, J.B. Fowlkes, J.L. Bull, Initial nucleation site formation due to acoustic droplet vaporization, *Appl. Phys. Lett.* 104 (6) (2014).
- [19] M.L. Fabiilli, C.G. Wilson, F. Padilla, F.M. Martin-Saavedra, J.B. Fowlkes, R.T. Franceschi, Acoustic droplet-hydrogel composites for spatial and temporal control of growth factor delivery and scaffold stiffness, *Acta Biomater.* 9 (7) (2013) 7399–7409.
- [20] M. Aliabouzar, C.D. Davidson, W.Y. Wang, O.D. Kripfgans, R.T. Franceschi, A.J. Putnam, J.B. Fowlkes, B.M. Baker, M.L. Fabiilli, Spatiotemporal control of micromechanics and microstructure in acoustically-responsive scaffolds using acoustic droplet vaporization, *Soft Matter* 16 (28) (2020) 6501–6513.
- [21] N.E. Hudson, J.R. Houser, E.T. O'Brien, R.M. Taylor 3rd, R. Superfine 2nd, S.T. Lord, M.R. Falvo, Stiffening of individual fibrin fibers equitably distributes strain and strengthens networks, *Biophys. J.* 98 (8) (2010) 1632–1640.
- [22] A. Moncion, M. Lin, E.G. O'Neill, R.T. Franceschi, O.D. Kripfgans, A.J. Putnam, M.L. Fabiilli, Controlled release of basic fibroblast growth factor for angiogenesis using acoustically-responsive scaffolds, *Biomaterials* 140 (2017) 26–36.
- [23] X. Lu, H. Jin, C. Quesada, E.C. Farrell, L.D. Huang, M. Aliabouzar, O.D. Kripfgans, J.B. Fowlkes, R.T. Franceschi, A.J. Putnam, M.L. Fabiilli, Spatially-directed cell migration in acoustically-responsive scaffolds through the controlled delivery of basic fibroblast growth factor, *Acta Biomater.* 113 (2020) 217–227.
- [24] L. Huang, C. Quesada, M. Aliabouzar, J.B. Fowlkes, R.T. Franceschi, Z. Liu, A.J. Putnam, M.L. Fabiilli, Spatially-directed angiogenesis using ultrasound-controlled release of basic fibroblast growth factor from acoustically-responsive scaffolds, *Acta Biomater.* 129 (2021) 73–83.
- [25] X. Huang, N. Yang, V.F. Fiore, T.H. Barker, Y. Sun, S.W. Morris, Q. Ding, V.J. Thannickal, Y. Zhou, Matrix stiffness-induced myofibroblast differentiation is mediated by intrinsic mechanotransduction, *Am. J. Respir. Cell Mol. Biol.* 47 (3) (2012) 340–348.
- [26] B. Hinz, The role of myofibroblasts in wound healing, *Curr. Res. Transl. Med.* 64 (4) (2016) 171–177.
- [27] R.T. Chitturi, A.M. Balasubramaniam, R.A. Parameswar, G. Kesavan, K.T. Haris, K. Mohideen, The role of myofibroblasts in wound healing, contraction and its clinical implications in cleft palate repair, *J. Int. Oral Health* 7 (3) (2015) 75–80.
- [28] L. Cai, W. Liu, Y. Cui, Y. Liu, W. Du, L. Zheng, C. Pi, D. Zhang, J. Xie, X. Zhou, Biomaterial stiffness guides cross-talk between chondrocytes: implications for a novel cellular response in cartilage tissue engineering, *ACS Biomater. Sci. Eng.* 6 (8) (2020) 4476–4489.
- [29] A.A. Gibb, M.P. Lazaropoulos, J.W. Elrod, Myofibroblasts and fibrosis: mitochondrial and metabolic control of cellular differentiation, *Circ. Res.* 127 (3) (2020) 427–447.
- [30] X. Tang, R. Peng, J.E. Phillips, J. Deguzman, Y. Ren, S. Apparsundaram, Q. Luo, C.M. Bauer, M.E. Fuentes, J.A. DeMartino, G. Tyagi, R. Garrido, C.M. Hogaboam, C.P. Denton, A.M. Holmes, C. Kitson, C.S. Stevenson, D.C. Budd, Assessment of Brd4 inhibition in idiopathic pulmonary fibrosis lung fibroblasts and in vivo models of lung fibrosis, *Am. J. Pathol.* 183 (2) (2013) 470–479.
- [31] Y.K. Jun, S.H. Kwon, H.T. Yoon, H. Park, H. Soh, H.J. Lee, J.P. Im, J.S. Kim, J.W. Kim, S.J. Koh, Toll-like receptor 4 regulates intestinal fibrosis via cytokine expression and epithelial-mesenchymal transition, *Sci. Rep.* 10 (1) (2020) 19867.
- [32] G. Raghun, H.R. Collard, J.J. Egan, F.J. Martinez, J. Behr, K.K. Brown, T.V. Colby, J.F. Cordier, K.R. Flaherty, J.A. Lasky, D.A. Lynch, J.H. Ryu, J.J. Swigris, A.U. Wells, J. Ancochea, D. Bours, C. Carvalho, U. Costabel, M. Ebina, D.M. Hansell, T. Johkoh, D.S. Kim, T.E. King Jr., Y. Kondoh, J. Myers, N.L. Muller, A.G. Nicholson, L. Richeldi, M. Selman, R.F. Dudden, B.S. Griss, S.L. Protzko, H.J. Schunemann, A.E.J.A.C.o.I.P. Fibrosis, An official ATS/ERS/JRS/ALAT statement: idiopathic pulmonary fibrosis: evidence-based guidelines for diagnosis and management, *Am. J. Respir. Crit. Care Med.* 183 (6) (2011) 788–824.
- [33] I.A. Darby, B. Laverdet, F. Bonte, A. Desmouliere, Fibroblasts and myofibroblasts in wound healing, *Clin. Cosmet. Investig. Dermatol.* 7 (2014) 301–311.
- [34] L.Y. Leung, D. Tian, C.P. Brangwynne, D.A. Weitz, D.J. Tschumperlin, A new microrheometric approach reveals individual and cooperative roles for TGF- $\beta$ 1 and IL-1 $\beta$  in fibroblast-mediated stiffening of collagen gels, *FASEB J.* 21 (9) (2007) 2064–2073.
- [35] N.M. Blythe, K. Muraki, M.J. Ludlow, V. Stylianidis, H.T.J. Gilbert, E.L. Evans, K. Cuthbertson, R. Foster, J. Swift, J. Li, M.J. Drinkhill, F.A. van Nieuwenhoven, K.E. Porter, D.J. Beech, N.A. Turner, Mechanically activated Piezo1 channels of

- cardiac fibroblasts stimulate p38 mitogen-activated protein kinase activity and interleukin-6 secretion, *J. Biol. Chem.* 294 (46) (2019) 17395–17408.
- [36] U. Nazet, S. Grassel, J. Jantsch, P. Proff, A. Schroder, C. Kirschneck, Early OA stage like response occurs after dynamic stretching of human synovial fibroblasts, *Int. J. Mol. Sci.* 21 (11) (2020).
- [37] Q. Meng, B. Bhandary, M.S. Bhuiyan, J. James, H. Osinska, I. Valiente-Alandi, K. Shay-Winkler, J. Gulick, J.D. Molkenin, B.C. Blaxall, J. Robbins, Myofibroblast-specific TGFbeta receptor II signaling in the fibrotic response to cardiac myosin binding protein C-induced cardiomyopathy, *Circ. Res.* 123 (12) (2018) 1285–1297.
- [38] L. Kubiczakova, L. Sedlarikova, R. Hajek, S. Sevcikova, TGF-beta - an excellent servant but a bad master, *J. Transl. Med.* 10 (2012) 183.
- [39] A. Leask, Potential therapeutic targets for cardiac fibrosis: TGFbeta, angiotensin, endothelin, CCN2, and PDGF, partners in fibroblast activation, *Circ. Res.* 106 (11) (2010) 1675–1680.
- [40] X. Lu, X. Dong, S. Natla, O.D. Kripfgans, J.B. Fowlkes, X. Wang, R. Franceschi, A.J. Putnam, M.L. Fabiilli, Parametric study of acoustic droplet vaporization thresholds and payload release from acoustically-responsive scaffolds, *Ultrasound Med. Biol.* 45 (9) (2019) 2471–2484.
- [41] M. Aliabouzar, A. Jivani, X.F. Lu, O.D. Kripfgans, J.B. Fowlkes, M.L. Fabiilli, Standing wave-assisted acoustic droplet vaporization for single and dual payload release in acoustically-responsive scaffolds, *Ultrason. Sonochem.* 66 (2020).
- [42] C.D. Markert, X. Guo, A. Skardal, Z. Wang, S. Bharadwaj, Y. Zhang, K. Bonin, M. Guthold, Characterizing the micro-scale elastic modulus of hydrogels for use in regenerative medicine, *J. Mech. Behav. Biomed. Mater.* 27 (2013) 115–127.
- [43] J.K. Gandhi, T. Knudsen, M. Hill, B. Roy, L. Bachman, C. Pfannkoch-Andrews, K.N. Schmidt, M.M. Metko, M.J. Ackerman, Z. Resch, J.S. Pulido, A.D. Marmorstein, Human fibrinogen for maintenance and differentiation of induced pluripotent stem cells in two dimensions and three dimensions, *Stem Cells Transl. Med.* 8 (6) (2019) 512–521.
- [44] N.J. Laping, E. Grygielko, A. Mathur, S. Butter, J. Bomberger, C. Tweed, W. Martin, J. Fornwald, R. Lehr, J. Harling, L. Gaster, J.F. Callahan, B.A. Olson, Inhibition of transforming growth factor (TGF)-beta1-induced extracellular matrix with a novel inhibitor of the TGF-beta type I receptor kinase activity: SB-431542, *Mol. Pharmacol.* 62 (1) (2002) 58–64.
- [45] D.L. Matera, K.M. DiLillo, M.R. Smith, C.D. Davidson, R. Parikh, M. Said, C.A. Wilke, I.M. Lombaert, K.B. Arnold, B.B. Moore, B.M. Baker, Microengineered 3D pulmonary interstitial mimetics highlight a critical role for matrix degradation in myofibroblast differentiation, *Sci. Adv.* 6 (37) (2020).
- [46] Z. Li, J.A. Dranoff, E.P. Chan, M. Uemura, J. Sevigny, R.G. Wells, Transforming growth factor-beta and substrate stiffness regulate portal fibroblast activation in culture, *Hepatology* 46 (4) (2007) 1246–1256.
- [47] P.D. Arora, N. Narani, C.A. McCulloch, The compliance of collagen gels regulates transforming growth factor-beta induction of alpha-smooth muscle actin in fibroblasts, *Am. J. Pathol.* 154 (3) (1999) 871–882.
- [48] Y. Asano, H. Ihn, K. Yamane, M. Jinnin, K. Tamaki, Increased expression of integrin alpha5beta5 induces the myofibroblastic differentiation of dermal fibroblasts, *Am. J. Pathol.* 168 (2) (2006) 499–510.
- [49] P.J. Wipff, D.B. Rifkin, J.J. Meister, B. Hinz, Myofibroblast contraction activates latent TGF-beta1 from the extracellular matrix, *J. Cell Biol.* 179 (6) (2007) 1311–1323.
- [50] P.A. Galie, M.V. Westfall, J.P. Stegemann, Reduced serum content and increased matrix stiffness promote the cardiac myofibroblast transition in 3D collagen matrices, *Cardiovasc. Pathol.* 20 (6) (2011) 325–333.
- [51] J.P.E. Junker, C. Kratz, A. Tollback, G. Kratz, Mechanical tension stimulates the transdifferentiation of fibroblasts into myofibroblasts in human burn scars, *Burns* 34 (7) (2008) 942–946.
- [52] S. Zhou, A. Schmelz, T. Seufferlein, Y. Li, J. Zhao, M.G. Bachem, Molecular mechanisms of low intensity pulsed ultrasound in human skin fibroblasts, *J. Biol. Chem.* 279 (52) (2004) 54463–54469.
- [53] N. Maeshige, H. Terashi, M. Aoyama, K. Torii, M. Sugimoto, M. Usami, Effect of ultrasound irradiation on alpha-SMA and TGF-beta1 expression in human dermal fibroblasts, *Kobe J. Med. Sci.* 56 (6) (2011) E242–E252.
- [54] Z. Fan, H. Liu, M. Mayer, C.X. Deng, Spatiotemporally controlled single cell sonoporation, *PNAS* 109 (41) (2012) 16486–16491.
- [55] I. Beekers, F. Mastik, R. Beurskens, P.Y. Tang, M. Vegter, A.F.W. van der Steen, N. de Jong, M.D. Verweij, K. Kooiman, High-resolution imaging of intracellular calcium fluctuations caused by oscillating microbubbles, *Ultrasound Med. Biol.* 46 (8) (2020) 2017–2029.
- [56] M.T. Burgess, T.M. Porter, Acoustic cavitation-mediated delivery of small interfering ribonucleic acids with phase-shift nano-emulsions, *Ultrasound Med. Biol.* 41 (8) (2015) 2191–2201.
- [57] S.M. Fix, A. Novell, Y. Yun, P.A. Dayton, C.B. Arena, An evaluation of the sonoporation potential of low-boiling point phase-change ultrasound contrast agents in vitro, *J. Ther. Ultrasound* 5 (2017) 7.
- [58] F. Robotti, S. Botton, F. Frascchetti, A. Mallone, G. Pellegrini, N. Lindenblatt, C. Starck, V. Falk, D. Poulidakos, A. Ferrari, A micron-scale surface topography design reducing cell adhesion to implanted materials, *Sci. Rep.* 8 (1) (2018) 10887.
- [59] M. Werner, S.B. Blanquer, S.P. Haimi, G. Korus, J.W. Dunlop, G.N. Duda, D.W. Grijpma, A. Petersen, Surface curvature differentially regulates stem cell migration and differentiation via altered attachment morphology and nuclear deformation, *Adv. Sci. (Weinh.)* 4 (2) (2017) 1600347.
- [60] P. Kollmannsberger, C.M. Bidan, J.W.C. Dunlop, P. Fratzl, V. Vogel, Tensile forces drive a reversible fibroblast-to-myofibroblast transition during tissue growth in engineered clefts, *Sci. Adv.* 4 (1) (2018).
- [61] S. Motte, L.J. Kaufman, Strain stiffening in collagen I networks, *Biopolymers* 99 (1) (2013) 35–46.
- [62] B.R. Seo, X. Chen, L. Ling, Y.H. Song, A.A. Shimpi, S. Choi, J. Gonzalez, J. Sapudom, K. Wang, R.C. Andresen Eguiluz, D. Gourdon, V.B. Shenoy, C. Fischbach, Collagen microarchitecture mechanically controls myofibroblast differentiation, *PNAS* 117 (21) (2020) 11387–11398.
- [63] O.D. Kripfgans, M.L. Fabiilli, P.L. Carson, J.B. Fowlkes, On the acoustic vaporization of micrometer-sized droplets, *J. Acoust. Soc. Am.* 116 (1) (2004) 272–281.
- [64] V.V. Petrov, R.H. Fagard, P.J. Lijnen, Stimulation of collagen production by transforming growth factor-beta1 during differentiation of cardiac fibroblasts to myofibroblasts, *Hypertension* 39 (2) (2002) 258–263.
- [65] E.E. Torr, C.R. Ngam, K. Bernau, B. Tomasini-Johansson, B. Acton, N. Sandbo, Myofibroblasts exhibit enhanced fibronectin assembly that is intrinsic to their contractile phenotype, *J. Biol. Chem.* 290 (11) (2015) 6951–6961.
- [66] M. Aliabouzar, X. Lu, O.D. Kripfgans, J.B. Fowlkes, M.L. Fabiilli, Acoustic droplet vaporization in acoustically-responsive scaffolds: effects of frequency of excitation, volume fraction, and threshold determination method, *Ultrasound Med. Biol.* 45 (12) (2019) 3246–3260.